ACS Photonics

pubs.acs.org/journal/apchd5

Article

Spectrally Encoded Nonscanning Imaging through a Fiber

Ningzhi Xie,[⊥] Quentin A. A. Tanguy,[⊥] Johannes E. Fröch, Karl F. Böhringer, and Arka Majumdar*

Cite This: https://doi.org/10.1021/acsphotonics.3c01582

Read Online

ACCESS | Metrics & More | Article Recommendations | Supporting Information

ABSTRACT: Recent advancements in neuroimaging and microsurgery have sparked an increasing demand to capture images with miniaturized optical probes such as optical fibers. In this work, we present an approach to acquire images through a single fiber without the need for mechanical scanning. At the distal end of the fiber, a metasurface filter array encodes spatial information into a highly orthogonal spectrum. At the proximal end, the object can then be computationally recovered via the pseudo inverse of the encoding process. We demonstrate captures of a 4 × 4 binary object at the proximity of the spectral filter array using a 560−625 nm wavelength band. The recovered image maintains an error rate of <11% when measured using a spectrometer with a spectral resolution of 1.5 nm. Importantly, this modality remains unchanged as the fiber is bent or moved. Thus, our approach shows a robust way to image through a single optical fiber, with potential applications in compact endoscopes and angioscopes.

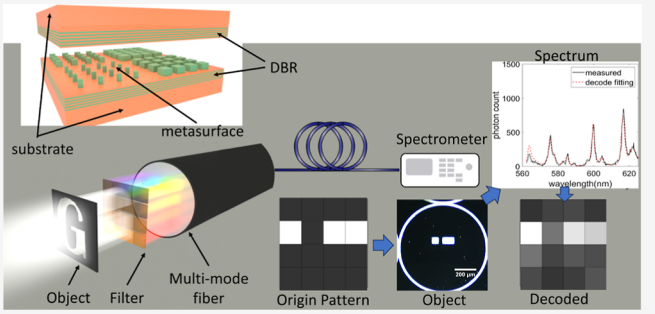

KEYWORDS: *metasurface, spectral encoding, spectral filter, fiber imaging, endoscope*

INTRODUCTION

Over the past half century, the concept of imaging through optical fibers has inspired an incessant drive in researchers to invent novel fiber-based imaging methods and apparatuses. The advent of neuroimaging and microsurgery has further increased this need for miniaturization and flexibility. The capability to see through a single optical fiber or a small bundle with extremely small device dimensions holds the potential to drastically transform the field of biomedical endoscopy, as sutureless surgery would become possible. Various approaches to this problem have been explored, including fiber-optic confocal microscopy,[1,2] scanning fiber endoscopy,[3,4] coherent fiber bundles,[5] and micro-electromechanical systems-scanned optical coherence tomography endoscopic probes.[6,7] In scanning-based modalities, an image is formed by scanning the fiber[3,8] or the beam at the distal end,[6,9] which results in bulky devices, relatively complicated integration, and low speed.[10,11] On the other hand, an ordered fiber array (i.e., a coherent fiber bundle)[12,13] enables direct imaging combined with a lens, but the resolution is ultimately limited by the number of fibers ∼10,000 in the bundle and typically has a larger diameter (∼1 mm).

To decrease the size of the optical probe to the ultimate limit, a range of imaging modalities utilizing single multimode fibers have been explored, with first experiments as early as the 1960s.[14] In this concept, one can exploit the fact that a multimode fiber transmits a larger number of optical modes simultaneously, which can be used to transmit more spatial information. The capability of imaging through a single fiber has been demonstrated via index profile engineering and modal phase compensation.[15,16] Recently, computational recovery of images captured through a multimode fiber have also been explored.[17] The fundamental idea is to model the propagation of the image through the multimode fiber using a transmission matrix and computationally reconstruct the image by inversion of this matrix. However, these methods lack robustness, and any disturbance or bending of the fiber necessitates recalibration of the transmission matrix.[18] More recently, a promising approach spatial-spectral encoding (SSE) has been reported,[19,20] where broadband light, incident at different angles or positions, is mapped to different spectra. In this case, the spectra is transmitted through the multimode fiber without any distortion and can be retrieved using a spectrometer at the proximal end. Through a computational decoding process, the intensity distribution at the distal end can thus be reconstructed. Such encoding methods have been demonstrated by using two orthogonally tilted Fabry−Pérot cavities[19] and a random scattering medium.[20]

However, in these earlier works, the spectra encoded to the light incident from distinct spatial pixels, known as the spectral codes, were broad-band and nondesignable. These codes contained high-frequency components that required a high-resolution (∼0.5 nm) spectral measurements.[19] Furthermore,

Received: October 31, 2023
Revised: February 8, 2024
Accepted: February 9, 2024

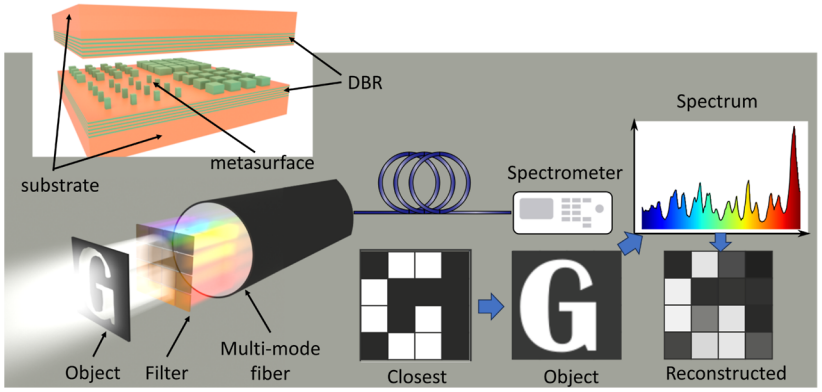

Figure 1. Schematic of a SSE device based on a spectral filter array. Inset: schematic of a metasurface phase-shifting layer wrapped in a FP cavity.

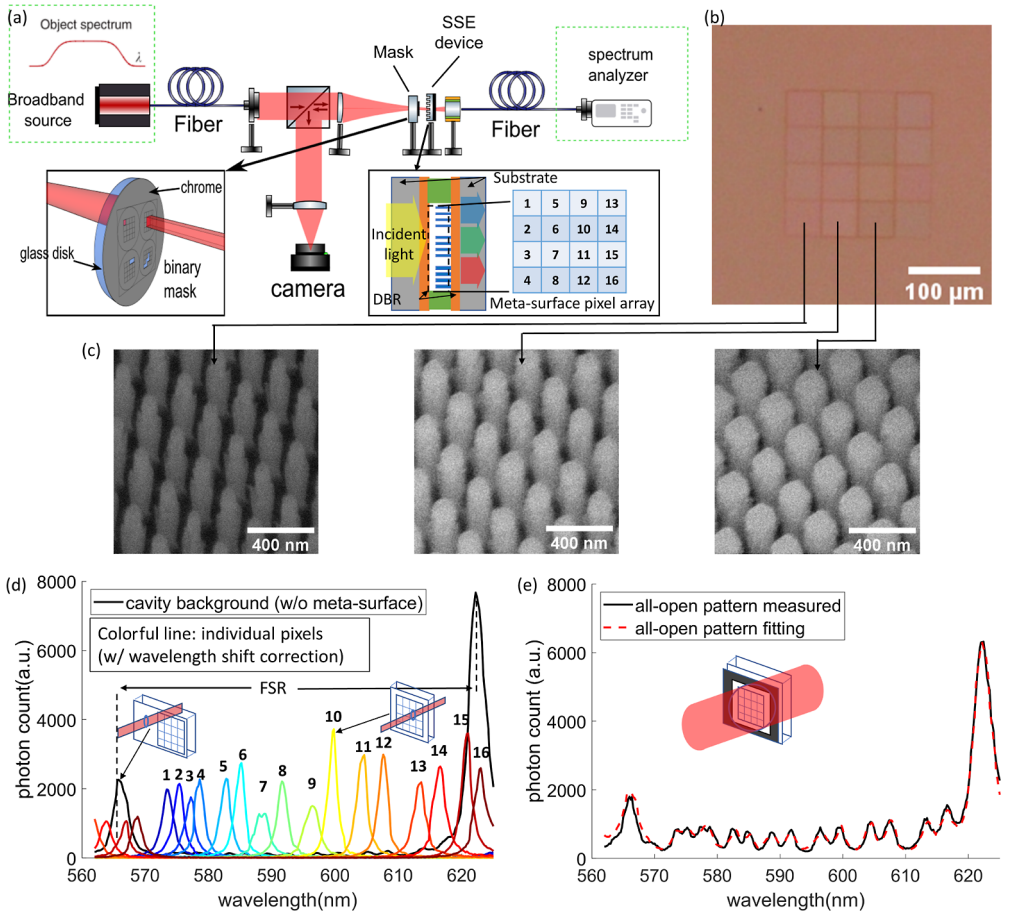

Figure 2. (a) Schematic of the experimental setup. The lower left inset shows the binary mask to generate various binary test patterns. The lower right inset depicts the cross-section of the SSE device. (b) Optical microscopy image of the SSE device. (c) SEM images of three different metasurfaces at an oblique angle of 40°. We note that images were taken before integration with the Fabry−Perot cavity. Metasurfaces from left to right were designed to impose phase-shifts of $\frac{1}{4}\pi$, $\frac{2}{4}\pi$, and $\frac{3}{4}\pi$, respectively. (d) The measured transmission spectra of 16 individual pixels of the SSE device (the spectral codes) in different colors from blue to red. These spectra are shifted to align to the corresponding resonance peaks of the transmission spectrum of the all-open pattern. The transmission spectrum of the cavity without metasurface (the background) is plotted (in black) for comparison. (e) The measured and fitting spectra of the all-open pattern. The fitting spectrum is the weight summation of the spectra codes.

as the codes were randomly generated, full post-fabrication calibration is crucial to achieve the desired spatial intensity reconstruction. This randomness also resulted in different spectral codes for different devices, requiring calibration of every device, hindering ubiquitous practical application of SSE. The randomized spectral codes also lacked orthogonality, leading to a high condition number for the spatial-spectral transfer matrix. As a result, the decoding process, which involved pseudo-inverting the transfer matrix, was sensitive to white noise and prone to improper calibration. Since the spectral codes were not designed, improving their orthogonality was challenging. Moreover, in these earlier works, the SSE optical devices are not compact, making integration with miniaturized imaging devices such as endoscopes difficult.

https://doi.org/10.1021/acsphotonics.3c01582
ACS Photonics XXXX, XXX, XXX−XXX

Fiber integrated spectrally encoded endoscopes using microgratings have also been demonstrated,[21,22] for which high spatial resolution was achieved. These works further explored the capability of endoscope integration and demonstrated fully assembled devices. However, the diffraction grating is fundamentally limited to spatial-to-spectral encoding in one dimension. Therefore, this approach ultimately required additional scanning mechanisms to acquire two-dimensional images.

Metasurfaces, quasi-periodic structures with subwavelength thickness and periodicity, can realize spatial and spectral modulation of light.[23] Moreover, metasurfaces have been integrated with fiber systems to realize beam focusing,[24] achromatic imaging,[2] endoscopic optical coherence tomography,[9] and quantitative phase imaging.[25] These characteristics make metasurfaces promising candidates for SSE in single fiber imaging.

By embedding a transmissive dielectric metasurface as a phase shifting element in a Fabry-Pérot (FP) cavity, a two-dimensional array of narrow band spectral filters with distinct passbands can be created,[26] which is suitable for SSE. As shown in the inset of Figure 1, the FP cavity is composed of two distributed Bragg reflectors (DBRs) facing each other. The metasurface phase shifter increases the effective optical path length of the FP cavity, red-shifting the transmitted resonant peak of the cavity. The spectral shift is proportional to the acquired phase shift in the metasurface, which can be engineered by the lateral size of the meta-atoms. A two-dimensional array of metasurfaces with varying phase shifts can thus function as a two-dimensional spectral filter array for spectrally encoded nonscanning single fiber imaging, featuring designable and highly orthogonal spectral codes. In addition, this DBR-metasurface-DBR spectral filter array is suitable for miniaturization and high-volume batch manufacturing. In particular, the metasurface can be fabricated in a scalable way by nanoimprint lithography.[27,28] We emphasize that such miniaturization is of utmost importance for an application like endoscopy, which requires placing such an optical system inside a living being.

In this work, we design and fabricate an SSE device based on this configuration and perform SSE and decoding experiments on 4 × 4 binary patterns in the wavelength range of 560−625 nm. By decoding the spectrum measured by a high-resolution (∼0.2 nm) spectrometer, we recover the binary patterns with an average error rate (defined as incorrect pixel assignment over total pixel number) of 9.8%. We further show that the error rate is maintained at 11% even when the spectral resolution of the measurement drops to ∼1.5 nm.

RESULTS AND DISCUSSION

Design of the SSE Device. The SSE device is a 4 × 4 spectral filter array with a pixel size of 50 μm × 50 μm, with each filter accommodating a distinct spectral and mutually orthogonal passband. A schematic of the metasurface-FP cavity is shown in the lower right inset of Figure 2a. Note that unlike similar devices previously reported,[26] we did not fully embed the metasurface in a polymer. Instead, we use SU8 as a spacer to effectively create an air pocket surrounding the metasurface. This ensures the largest possible index contrast for the SiN meta-atoms. Otherwise, the relatively low refractive index of ∼2.0 would reduce the index contrast, making it harder to impose the required range of phase delays on transmitted light.

Ensuring orthogonality between spectral codes is a key factor of the SSE and can be achieved by distributing the FP resonances evenly across the full free spectral range (FSR) of the FP cavity.[19] We engineer the phase delay of each pixelate metasurface (ϕ_i) to effectively increase the round-trip phase delay of the cavity, ψ, by $2\phi_i$, thus shifting the resonance wavelength λ_i. To form a resonant mode in a DBR-metasurface-DBR cavity, the round-trip phase ψ must satisfy

$$\psi = 2\left(\phi_i + \frac{2\pi}{\lambda_i}L\right) = 2\pi q \tag{1}$$

where L is the cavity length and q is an integer corresponding to the order of the resonance mode, assuming the light incident on the filter is a plane wave at normal incidence. We set L = 2.5 μm, and use the resonance at q = 9. The transmission peak wavelength for each filter can be written as

$$\lambda_i = \frac{2L}{q - \phi_i/\pi} = \frac{2L}{q} + \frac{2L}{q^2}\frac{\phi_i}{\pi} + \frac{2L}{(q - \phi_i/\pi)q^2}\left(\frac{\phi_i}{\pi}\right)^2 \tag{2}$$

The FSR is given by the difference between two adjacent orders

$$\Delta\lambda_{\mathrm{FSR}} = \frac{2L}{q-1} - \frac{2L}{q} = \frac{2L}{q^2} + \frac{2L}{(q-1)q^2} \tag{3}$$

The resonances λ_i of the spectral filters should be confined within one FSR to avoid any overlap with resonances of different orders. Thus, from eqs 2 and 3, we conclude that the metasurface phase delay ϕ_i must range from 0 to π. With $q \gg 1$ and $\phi_i \in (0, \pi)$, λ_i can be approximated as $\frac{2L}{q} + \frac{2L}{q^2}\frac{\phi_i}{\pi} = 555.6\ \mathrm{nm} + \frac{\phi_i}{\pi}\cdot 61.7\ \mathrm{nm}$, which is close to the design wavelength λ_d = 560 nm and increases linearly with $\frac{\phi_i}{\pi}$. As $\frac{\phi_i}{\pi} \in (0, 1)$, the error term of this approximation, $\frac{2L}{(q-\phi_i/\pi)q^2}\left(\frac{\phi_i}{\pi}\right)^2$, has an upper bound $\frac{2L}{(q-1)q^2}\frac{\phi_i}{\pi} = \frac{\phi_i}{\pi}\cdot 7.7\ \mathrm{nm}$, which is 8 times smaller compared to the linear term. Therefore, this error term has a negligible effect on the linearity of λ_i as a function of ϕ_i. As a result, to uniformly cover the FSR, ϕ_i should range from 0 to π with equal intervals. We choose a meta-atom with appropriate height, periodicity, and width to cover the 0−π phase range at this wavelength range. Design and simulation of the metasurfaces is further detailed in the Methods section. The simulated phase delay of the meta-atom as a function of lateral size and wavelength is shown in the Figure S1. Fabrication details can also be found in the Methods section. Figure 2b shows an optical image of the fabricated SSE device from the top, while Figure 2c shows scanning electron microscopy (SEM) images of three different metasurface pixels, whereas for each structure, the meta-atoms have different lateral sizes to impose different phase delays to the light.

Experimental Setup. To demonstrate the functionality of the metasurface SSE, we placed a sample containing a variation of 4 × 4 pixel binary objects in front of the filter (distance ∼0.1 mm). Each individual binary object is a patterned chrome film, with each pixel either being transparent or blocking light, whereas each pixel has the same lateral dimensions as the SSE metasurface filter array. Light from a laser beam was then directed onto the binary mask, whereas only transparent

https://doi.org/10.1021/acsphotonics.3c01582
ACS Photonics XXXX, XXX, XXX−XXX

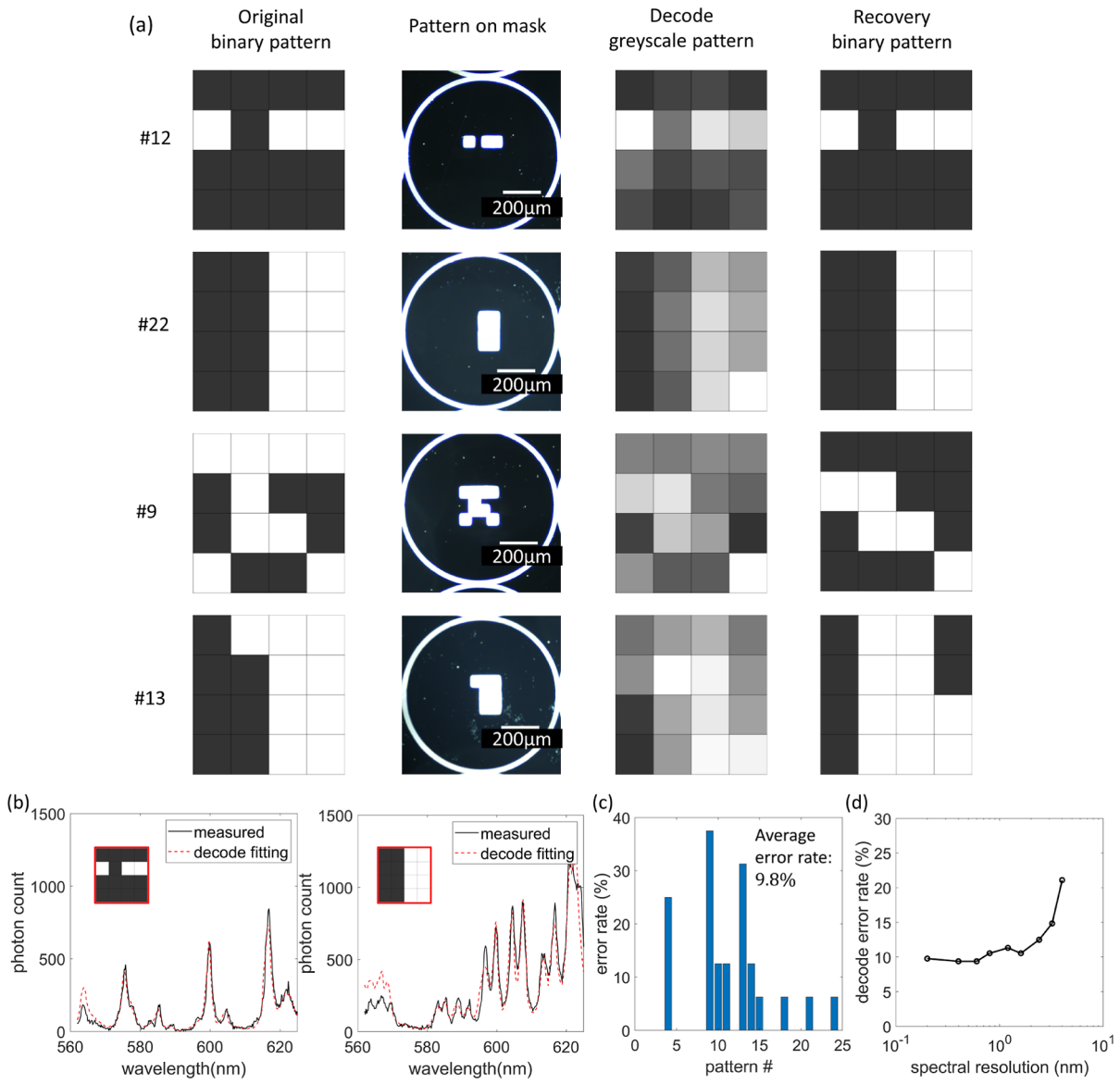

Figure 3. (a) 12th, 22nd, 9th, and 13th original binary patterns, the microscope image of the corresponding binary patterns on the chrome mask, the decoded grayscale patterns, and the recovered binary pattern from the decoded grayscale patterns. The threshold is set at the midpoint of the minimal and maximal greyscale values. (b) The spectra of the 12th and 22nd patterns. The number of data points of the spectra is 316, for decoding 16 spatial pixels. (c) The error rates of the 24 recovered binary patterns compared to the original patterns using the high resolution (0.2 nm) measured spectra data, which contains ≈20 spectrum data points per spatial pixels. (d) The pattern recovery average error rates (over 24 patterns) as a function of the resolution of the pattern spectra.

portions appear bright (see Figure 2a). The width of the laser beam in the focal plane of the sample is large enough to cover the full pattern. Thus, as light from the object passes through the SSE device, spatial pixel information is encoded into a unique spectral code. The spectrally encoded light was coupled into the optical fiber, which was connected to a spectrometer to measure the transmitted spectrum. Detailed information on the setup can be found in the Methods section. After measurement, the spectrum is computationally decoded to recover the pattern of the object using a pseudo inverse of the matrix **M** containing the superposed spectral codes. To minimize the cross-coupling between the spectral codes, the columns of matrix **M** should be as orthogonal as possible.

Decoding. The SSE process can be described as $b = \mathbf{M}a$, where a represents the $m \times 1$ vector of the input pixel values of a pattern, and b the $n \times 1$ spectral output.[19] **M** is the spectral encoding transfer matrix. Each column of **M** is the spectral code of one of the corresponding spatial pixel. Decoding consists in retrieving the input pattern a, which can be achieved by pseudo inverse of **M**: $a = \mathbf{M}^{\dagger}b$, where $\mathbf{M}^{\dagger}$ is the pseudoinverse of matrix **M**. The details of the decoding algorithm can be found in the Supporting Information.

To retrieve the spatial input, we first characterize **M** by measuring the transmission spectra of all 16 single pixels of the SSE device (i.e., the spectral codes). We also measured the transmission spectrum of the bare device in the absence of a phase shifting metasurface. As discussed before, we chose the wavelength range 560−625 nm for computational decoding, which corresponds to the FSR of the FP cavity and covers the resonance peaks of all 16 pixels (see Figure S2). The measured spectral codes and background within this wavelength range are plotted in Figure 2d. As can be seen in this figure, the peaks

https://doi.org/10.1021/acsphotonics.3c01582
ACS Photonics XXXX, XXX, XXX−XXX

of the spectral codes are well separated with minimal overlap, indicating a high orthogonality. We note that the intensity peaks corresponding to the last two pixels overlap with the signal of the bare cavity, as the metasurface phase shift of these two pixels is close to π. However, the effect of this overlap can be corrected by including it as a background signal in the decoding process.

We note that the measured spectral codes are slightly shifted and modulated in their amplitude as compared to the spectrum of the all-open pattern (see Figure S4). Therefore, we calibrated transfer matrix **M** by fitting the measured spectrum of the all-open pattern using the measured spectral codes and background. We shifted the measured spectral codes in wavelength to align to the resonance peaks of the spectrum of the all-open pattern, and add weight factors to modulate the relative amplitude of the spectral codes. The calibration details are reported in Section S3. The fitted spectrum of the all-open pattern is plotted in Figure 2e (red dashed line), which matches well with the measured spectrum (black solid line).

Using calibrated transfer matrix **M** and the decoding method described above, we recovered the binary intensity patterns from the measured spectra of 24 different original patterns. Figure 3a shows four examples of the binary pattern decoding process with the SSE. The first two patterns are recovered without error, while the last two patterns are the most erroneous among all measured patterns. The decoding process for all 24 original patterns are summarized in Figure S5.

To quantitatively evaluate the fidelity of the imaging approach, we define an error rate as the number of pixels that are incorrectly reconstructed divided by the total number of pixels. The error rates for all of the binary patterns are plotted in Figure 3c. We used a high resolution (0.2 nm) spectrometer with $n = 316$ data points in the wavelength range of 562−625 nm (20 spectral data points per spatial pixel). This results in an average error rate of 9.8%. We further investigated the dependency of the decoding error rate on the resolution of the pattern spectra. We synthesized low-resolution spectral data by artificially compressing the number of data points of the measured pattern spectra and the spectral codes, and repeated the computational decoding on these low-resolution pattern spectra. As seen in Figure 3d, the decoding error rate only marginally increases when the spectral resolution decreases. As long as the resolution is better than 1.5 nm the error rate is maintained below ∼11%. This shows that with our SSE, the decoding can be efficiently performed using a low-resolution spectrometer. In addition, once the transfer matrix **M** is calibrated, the decoding process can be achieved by a computationally efficient matrix multiplication, which facilitates real-time imaging.

While most patterns are accurately reconstructed (one or less incorrect pixel assignment), some (particularly ninth and 13th, Figure 3a) yield extremely high error rates, which contributed most to the ∼10% average error rate of the spatial-spectral decoding experiment. This high error rate may stem from lateral misalignment between pixels of the binary patterns and the SSE device, as illustrated in Figure 4a. For example, for the 13th pattern, we observe that the recovered pattern yields a similar shape as the original pattern but translated to the left by one pixel, indicating misalignment between the pattern and the SSE device during the measurement. The high error rate of the ninth pattern could be caused by the divergence of light transmitted through the pattern. Our SSE device is based on the assumption that the incident light is a plane wave. This

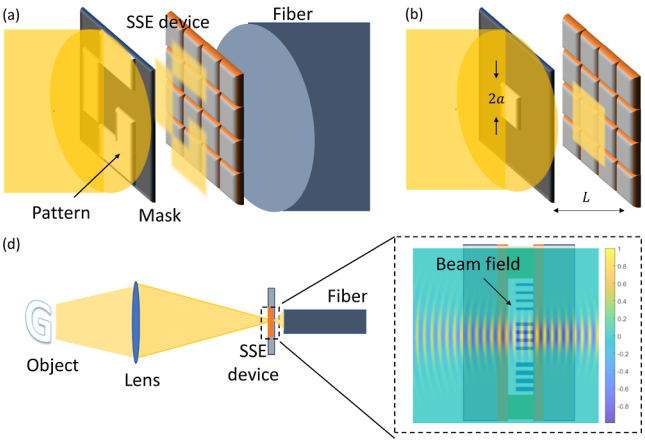

Figure 4. (a) Pixel misalignment between the binary pattern on the mask and the SSE. (b) Pixel broadening in SSE near field imaging.(c) Scheme for far-field imaging through a lens and the SSE device.

assumption is satisfied under near-field imaging condition, where the Fresnel number $F = a^2/\lambda L \gg 1$. In our experiment setup, the characteristic length for a single pixel of the pattern is half the size of the pixel, $a = 25$ μm, the propagation distance $L \approx 600$ μm (slightly thicker than the substrate 500 μm), and the wavelength $\lambda \approx 560$ nm. These parameters give a Fresnel number of $F \approx 1.8$, which indicates that we expect the light beam to diverge. Essentially, as described in Figure 4b, the light from one single pixel of the pattern on the mask could leak to the surrounding pixels of the SSE device. For the ninth pattern, it has a long contour length so that the leaking of the light to the surrounding pixel results in a more erroneous pixel in the recovery pattern. The nonideal plane wave incident of the light can cause deformations of the resonance transmission peaks of the cavity (the spectral codes of the SSE), which may also result in decoding errors.

The near field condition becomes harder to satisfy as the pixel size decreases because the near field distance ($F > 1$) is proportional to the square of the pixel size. In order to satisfy the near-field condition, for a pixel size of 2 μm ($a = 1$ μm), the working distance between the object and the filter would have to be smaller than 1.8 μm, thus limiting the applications of SSE in microscopy. On the other hand, as shown in Figure 4c, the beam focused by a lens (Gaussian pilot beam) can be considered a plane wave near the focal point within a range defined by the Rayleigh length $Z_R = \pi w_0^2/\lambda$. For a pixel size of 2 μm ($w_0 = 1$ μm), $Z_R = 5.6$ μm, which is larger than the thickness of the SSE device. When the SSE device is placed within this range, the plane wave condition is satisfied. Therefore, by using a focusing lens, we can potentially image in the far field via spectral encoding through the SSE device, even if the pixel size of the SSE is reduced to 2 μm.

For filter-based SSE devices with completely orthogonal spectral codes, the overall optical efficiency is limited to $\sim 1/N$, where N is the number of spectral filters (pixels), assuming a transmission of 100% at $1/N$ of the whole working band and a transmission of 0 at the other wavelengths. Thus, for our case of $N = 16$, the highest possible collection efficiency for a single pixel is 6.67%. We simulated an optical efficiency of 3.73% (56% of the limit) and estimate the experimental optical efficiency to be 1.85% (28% of the limit). Calculation details are summarized in Section S2.

https://doi.org/10.1021/acsphotonics.3c01582
ACS Photonics XXXX, XXX, XXX−XXX

Unlike the binary mask studied in this work, most biological objects have a spatially varying spectral response. This, however, may not significantly impact the SSE functionality as long as the spectral response of the object does not drastically vary (i.e., strong absorption line or fluorescence emission) across the operating wavelength range. Because the spectral codes of our SSE are narrow band, the value of a specific pixel of the reconstructed image is mainly determined by the local spectrum near the resonant wavelength of that pixel. Thus, the impact of the spectral information on the object to the reconstructed image will virtually be that of a weak amplitude filter.

Although the small pixel number (16) of our SSE device limits its application for conventional imaging, some laser guided surgeries require as little as 3 pixels to navigate the movement of surgical instruments.[29] Thus, an SSE device with only 16 pixels can already be useful and potentially replace the previously used multicore fibers for collecting such information, while being thinner, cheaper, more robust, and easier to integrate.

We further note that the number of pixels in our current device is limited by the FSR of the FP cavity over the resonance width of the filter, i.e., the Q factor of the cavity. Therefore, we could increase the number of pixels by engineering the cavity Q-factor, or using photonic crystal spectral filters with high Q resonances.[30] In addition, by implementing compressive sensing strategies, the number of pixels could be further improved to an extent that exceeds the limits imposed by the Q factor of the spectral filters. Another straightforward way to increase the number of pixels is to employ multiple fibers, whereas each fiber captures a low-resolution image. Given that each fiber is very thin, we can capture a large number of pixels with an array. Unlike in a coherent fiber bundle, each fiber will collect 16 pixels, allowing an order of magnitude increase in the number of pixels with the same number of fiber cores. This method affords a novel approach in guiding medical interventions which is placing the 2−4 imaging fibers individually around the disposable tool, such as 2 on either side of forceps and 4 around the perimeter of a suction or cautery catheter device.

CONCLUSIONS

We designed and fabricated an SSE device with a controllable spectral code using a spectral filter array. This device is composed of metasurfaces integrated with a FP cavity, whereas a nonlocal metasurface imparts a desired phase shift to locally change the transmission band. With this SSE device, we perform a SSE and decoding experiment through a single multimode fiber, imaging 4 × 4 pixel binary patterns (pixel size of 50 μm × 50 μm). These binary patterns are implemented as a transmissive mask, which is placed at the near field of the SSE device. Light is encoded and collected by the device, which are then measured at the proximal end of the fiber and decoded to recover the binary patterns by least-squares fitting using the summation of the spectral codes of the SSE. The decoded patterns have an average error rate of 9.7% when the pattern spectra has a high resolution of 0.2 nm (the number of data points of spectra is 20 × the number of pixels of the patterns). This error rate is maintained at ≈11% even at a much lower spectral resolution of 1.5 nm (the spectral number of data point is 2.5 × the number of pixels). Therefore, spectra could be recorded by a cheaper, miniaturized, low-resolution spectrometer. This miniaturized SSE device, when integrated with an optical fiber, can function as an endoscope with an ultrasmall diameter and short rigid tip length.

Even though our encoding of the patterns is performed under near field condition, far field imaging and encoding through our SSE device is possible by putting the SSE at the focal plane of a lens. For far field imaging, the size of the pixel of the SSE can possibly be reduced to 2 μm × 2 μm. While our SSE device only has 16 pixels, it could still be useful in applications such as laser-guided surgeries. The number of pixels of the SSE could be further increased by using a cavity with higher Q factors, a photonic crystal spectral filter with high Q resonance, or employing a fiber array.

METHODS

Experimental Setup. Broadband light (Thorlab High-Power Stabilized Quartz Tungsten-Halogen Source: 360−2500 nm, SLS302) is coupled to an optical fiber, then collimated by a tube lens (Thorlab AC254-030-A-ML, f = 30 mm) at the fiber output, and subsequently focused by an objective onto the binary pattern mask and/or the SSE device. For the transmission spectral measurements of individual pixels of the SSE device, we used a fiber with core diameter: 10 μm (Thorlabs M64L01, 0.1 NA), the objective: Nikon LU Plan Fluor 10×, WD = 17.5 mm, NA = 0.30, the beam size on the SSE device: ≈ 20 μm. For the transmission spectral measurements of the binary patterns on the mask, the fiber core diameter: 200 μm (Thorlabs M122L02, 0.22 NA), the objective: Nikon LU Plan Fluor 5×, WD = 23.5 mm, NA = 0.15, the beam size on the mask: ∼800 μm. A 50/50 beam splitter is placed in between the collimator and the objective, combined with a tube lens (Thorlabs AC254-100-A-ML, f = 100 mm) and a camera (Thorlabs CS165CU) for viewing the patterns on the mask. The binary patterns on the mask are created by photolithography. The light transmitted through the SSE device is coupled to another fiber (Thorlabs M74L05, core diameter = 400 μm, 0.39 NA), which is connected to a spectrometer (Teledyne Princeton Instruments, IsoPlane SCT 320) for spectral measurements of light coupled to the fiber.

Design of the Metasurface. The metasurface consists of a 4 × 4 pixel array, where each pixel is 50 × 50 μm square. The metasurface is made of Si_3N_4 square meta-atoms on a fused silica substrate (height = 500 nm, square lattice, pitch = 300 nm). The size of the meta-atoms for each individual pixel is selected to satisfy the phase shift requirement: for the ith pixel, the (single pass) phase shift is $\frac{i}{16}\pi$ at the resonance wavelength of the FP cavity of that pixel. We use rigorous coupled-wave analysis[31] to theoretically calculate the phase delay as a function of the meta-atom lateral size and wavelength. The results are shown in Figure S1.

These two DBRs are bonded together with a spacing of 2.5 μm, which defines the cavity length L, using the SU8 resist as the bonding material and the spacer.

Fabrication of the SSE Device. The two DBRs are grown on two 500 μm thick fused-silica substrates (10 × 10 mm^2 chip) with plasma-enhanced chemical vapor deposition. These DBRs are made of seven alternating layers of Si_3N_4 (n = 1.97 at 560 nm, thickness = 71 nm) and SiO_2 (n = 1.44 at 560 nm, thickness = 97 nm), which have a reflecting band centered at 560 nm. After that, 500 nm Si_3N_4 is deposited on one of the DBRs, where the metasurface is fabricated by electron beam lithography (EBL). A 300 nm thick e-beam resist (ZEP-520A) is spin-coated and patterned by EBL, and then, a ≈ 65 nm

https://doi.org/10.1021/acsphotonics.3c01582
ACS Photonics XXXX, XXX, XXX−XXX

thick Al_2O_3 hard mask is created by electron beam assisted evaporation followed by resist lift-off in *N*-methyl-2-pyrrolidone at 90 °C overnight. Subsequently, the Si_3N_4 layer is etched by a fluorine-based reactive ion process. Meanwhile, a 2.5 μm thick SU8 resist is spin-coated on the other DBR and patterned by photolithography to create a spacer structure (a ring with inner diameter = 5 mm, outer diameter = 8 mm, and height = 2.5 μm). Finally, the two DBRs are bonded together with metasurface wrapped inside using a flip-chip bonder. The SU8 bonding is done by heating up the two substrates to 250 °C and applying 40 N force for 1 h. The sketch of the process flow can be seen in Figure S6.

■ ASSOCIATED CONTENT

Supporting Information

The Supporting Information is available free of charge at https://pubs.acs.org/doi/10.1021/acsphotonics.3c01582.

Simulated phase delay of the meta-atom as a function of pitch, lateral size, and incident light wavelength; raw measurement data of the transmission spectra of each pixel of the SSE device and the encoded patterns; mathematical description of the decoding algorithm; calibration of the spectral code; decoding process of all 24 binary patterns; and sketch of the fabrication process flow of the SSE device (PDF)

■ AUTHOR INFORMATION

Corresponding Author

Arka Majumdar − *Department of Electrical and Computer Engineering, University of Washington, Seattle, Washington 98195, United States; Department of Physics, University of Washington, Seattle, Washington 98195, United States;* orcid.org/0000-0003-0917-590X; Email: arka@uw.edu

Authors

Ningzhi Xie − *Department of Electrical and Computer Engineering, University of Washington, Seattle, Washington 98195, United States;* orcid.org/0009-0001-7484-7808

Quentin A. A. Tanguy − *Department of Electrical and Computer Engineering, University of Washington, Seattle, Washington 98195, United States*

Johannes E. Fröch − *Department of Electrical and Computer Engineering, University of Washington, Seattle, Washington 98195, United States; Department of Physics, University of Washington, Seattle, Washington 98195, United States*

Karl F. Böhringer − *Department of Electrical and Computer Engineering, University of Washington, Seattle, Washington 98195, United States; Department of Bioengineering and Institute for Nano-engineered Systems, University of Washington, Seattle, Washington 98195, United States;* orcid.org/0000-0002-9428-2648

Complete contact information is available at: https://pubs.acs.org/10.1021/acsphotonics.3c01582

Author Contributions

⊥N.X. and Q.A.A.T contributed equally to this work.

Funding

The work was supported by NSF GCR 2120774. The Washington nanofabrication facility/molecular analysis facility where part of this work was conducted is partially supported by the National Science Foundation (NSF) via awards NNCI-1542101 and NNCI-2025489.

Notes

The preprint version of this manuscript has been submitted to arXiv.org: Xie, N.; Tanguy, Q.; Fröch, J.; Böhringer, K.; Majumdar, A. Spectrally-encoded non-scanning imaging through a fiber. 2023, arXiv: 2305.17113.

The authors declare the following competing financial interest(s): Arka Majumdar and Karl F. Bhringer are co-founder of Tunoptix, which is looking into commercializing metaoptics.

■ ACKNOWLEDGMENTS

Part of this work was conducted at the Washington Nanofabrication Facility/Molecular Analysis Facility, a National Nanotechnology Coordinated Infrastructure (NNCI) site at the University of Washington supported by NSF grants ECCS-2025489 and ECCS-1542101.

■ REFERENCES

(1) Dabbs, T.; Glass, M. Fiber-optic confocal microscope: FOCON. *Appl. Opt.* **1992**, *31*, 3030−3035.

(2) Ren, H. R.; Jang, J.; Li, C. H.; Aigner, A.; Plidschun, M.; Kim, J.; Rho, J.; Schmidt, M. A.; Maier, S. A. An achromatic metafiber for focusing and imaging across the entire telecommunication range. *Nat. Commun.* **2022**, *13*, 4183.

(3) Lee, C. M.; Engelbrecht, C. J.; Soper, T. D.; Helmchen, F.; Seibel, E. J. Scanning fiber endoscopy with highly flexible, 1 mm catheterscopes for wide-field, full-color imaging. *J. Biophotonics* **2010**, *3*, 385−407.

(4) Xie, N.; Carson, M. D.; Fröch, J. E.; Majumdar, A.; Seibel, E.; Böhringer, K. F. Large FOV short-wave infrared meta-lens for scanning fiber endoscopy. *J. Biomed. Opt.* **2023**, *28*, 094802.

(5) Hirschowitz, B. I.; Curtiss, L. E.; Peters, C. W.; Pollard, H. M. Demonstration of a New Gastroscope, the Fiberscope. *Gastroenterology* **1958**, *35*, 50−53.

(6) Struk, P.; Bargiel, S.; Tanguy, Q. A. A.; Garcia Ramirez, F. E.; Passilly, N.; Lutz, P.; Gaiffe, O.; Xie, H.; Gorecki, C. Swept-source optical coherence tomography microsystem with an integrated Mirau interferometer and electrothermal micro-scanner. *Opt. Lett.* **2018**, *43*, 4847.

(7) Duan, C.; Tanguy, Q.; Pozzi, A.; Xie, H. Optical coherence tomography endoscopic probe based on a tilted MEMS mirror. *Biomed. Opt. Express* **2016**, *7*, 3345−3354.

(8) Seo, Y.-H.; Hwang, K.; Jeong, K.-H. 165 mm diameter forward-viewing confocal endomicroscopic catheter using a flip-chip bonded electrothermal MEMS fiber scanner. *Opt. Express* **2018**, *26*, 4780.

(9) Pahlevaninezhad, H.; Khorasaninejad, M.; Huang, Y. W.; Shi, Z.; Hariri, L. P.; Adams, D. C.; Ding, V.; Zhu, A.; Qiu, C. W.; Capasso, F.; Suter, M. J. Nano-optic endoscope for high-resolution optical coherence tomography in vivo. *Nat. Photonics* **2018**, *12*, 540−547.

(10) Kim, D. Y.; Hwang, K.; Ahn, J.; Seo, Y. H.; Kim, J. B.; Lee, S.; Yoon, J. H.; Kong, E.; Jeong, Y.; Jon, S.; Kim, P.; Jeong, K. H. Lissajous Scanning Two-photon Endomicroscope for In vivo Tissue Imaging. *Sci. Rep.* **2019**, *9*, 3560.

(11) Tanguy, Q. A. A.; Gaiffe, O.; Passilly, N.; Cote, J.-M.; Cabodevila, G.; Bargiel, S.; Lutz, P.; Xie, H.; Gorecki, C. Real-time Lissajous imaging with a low-voltage 2-axis MEMS scanner based on electrothermal actuation. *Opt. Express* **2020**, *28*, 8512.

(12) Miyoshi, Y.; Nishimura, T.; Shimojo, Y.; Okayama, K.; Awazu, K. Endoscopic image-guided laser treatment system based on fiber bundle laser steering. *Sci. Rep.* **2023**, *13*, 2921.

(13) Fröch, J. E.; Huang, L.; Tanguy, Q. A. A.; Colburn, S.; Zhan, A.; Ravagli, A.; Seibel, E. J.; Böhringer, K. F.; Majumdar, A. Real time full-color imaging in a Meta-optical fiber endoscope. *eLight* **2023**, *3*, 13.

(14) Spitz, E.; Werts, A. Transmission des images à travers une fibre optique. *C. R. Acad. Sci. B* **1967**, *264*, 1015.

(15) Yariv, A. Three-dimensional pictorial transmission in optical fibers. *Appl. Phys. Lett.* **1976**, *28*, 88−89.

(16) Friesem, A.; Levy, U.; Silberberg, Y. Parallel transmission of images through single optical fibers. *Proc. IEEE* **1983**, *71*, 208−221.
(17) Choi, Y.; Yoon, C.; Kim, M.; Yang, T. D.; Fang-Yen, C.; Dasari, R. R.; Lee, K. J.; Choi, W. Scanner-Free and Wide-Field Endoscopic Imaging by Using a Single Multimode Optical Fiber. *Phys. Rev. Lett.* **2012**, *109*, 203901.
(18) Popoff, S. M.; Lerosey, G.; Carminati, R.; Fink, M.; Boccara, A. C.; Gigan, S. Measuring the transmission matrix in optics: An approach to the study and control of light propagation in disordered media. *Phys. Rev. Lett.* **2010**, *104*, 100601.
(19) Barankov, R.; Mertz, J. High-throughput imaging of self-luminous objects through a single optical fibre. *Nat. Commun.* **2014**, *5*, 5581.
(20) Kolenderska, S. M.; Katz, O.; Fink, M.; Gigan, S. Scanning-free imaging through a single fiber by random spatio-spectral encoding. *Opt. Lett.* **2015**, *40*, 534−537.
(21) Kang, D.; Martinez, R. V.; Whitesides, G. M.; Tearney, G. J. Miniature grating for spectrally-encoded endoscopy. *Lab Chip* **2013**, *13*, 1810−1816.
(22) Zeidan, A.; Do, D.; Kang, D.; Ikuta, M.; Ryu, J.; Tearney, G. J. High-Resolution, Wide-Field, Forward-Viewing Spectrally Encoded Endoscope. *Lasers Surg. Med.* **2019**, *51*, 808−814.
(23) Bukhari, S. S.; Vardaxoglou, J.; Whittow, W. A Metasurfaces Review: Definitions and Applications. *Appl. Sci. Basel* **2019**, *9*, 2727.
(24) Yang, J. Y.; Ghimire, I.; Wu, P. C.; Gurung, S.; Arndt, C.; Tsai, D. P.; Lee, H. W. H. Photonic crystal fiber metalens. *Nanophotonics* **2019**, *8*, 443−449.
(25) Shanker, A.; Froech, J.; Mukherjee, S.; Zhelyeznyakov, M.; Seibel, E.; Majumdar, A. Quantitative Phase Imaging with a Metalens. *arXiv* **2023**, arXiv.2309.11348.
(26) Horie, Y.; Arbabi, A.; Arbabi, E.; Kamali, S. M.; Faraon, A. Wide bandwidth and high resolution planar filter array based on DBR-metasurface-DBR structures. *Opt. Express* **2016**, *24*, 11677−11682.
(27) Kim, J.; Seong, J.; Kim, W.; Lee, G. Y.; Kim, S.; Kim, H.; Moon, S. W.; Oh, D. K.; Yang, Y.; Park, J.; et al. Scalable manufacturing of high-index atomic layer-polymer hybrid metasurfaces for metaphotonics in the visible. *Nat. Mater.* **2023**, *22*, 474−481.
(28) Choi, H.; Kim, J.; Kim, W.; Seong, J.; Park, C.; Choi, M.; Kim, N.; Ha, J.; Qiu, C. W.; Rho, J.; Lee, H. Realization of high aspect ratio metalenses by facile nanoimprint lithography using water-soluble stamps. *Photonix* **2023**, *4*, 18.
(29) Swanson, E. Multicore Fiber Instrument with 3D-Printed Distal Optics. U.S. Patent 16/864,056, 2021.
(30) Wang, Z.; Yi, S.; Chen, A.; Zhou, M.; Luk, T. S.; James, A.; Nogan, J.; Ross, W.; Joe, G.; Shahsafi, A.; Wang, K. X.; Kats, M. A.; Yu, Z. F. Single-shot on-chip spectral sensors based on photonic crystal slabs. *Nat. Commun.* **2019**, *10*, 1020.
(31) Liu, V.; Fan, S. S4: A free electromagnetic solver for layered periodic structures. *Comput. Phys. Commun.* **2012**, *183*, 2233−2244.

https://doi.org/10.1021/acsphotonics.3c01582
ACS Photonics XXXX, XXX, XXX−XXX